

Beyond Maxwell-Boltzmann statistics using confined vapor cells

Gilad Orr¹ and Eliran Talker^{*2}

¹Department of Physics, Ariel University, Ariel 40700

²Department of Electrical Engineering, Ariel University, Ariel 40700, Israel

June 7, 2025

Abstract

Coherence time of thermal photons in rubidium vapor cells with varying thicknesses, reveal that there is clear dependence of the photon correlation time on cell thickness. Standard theoretical models accurately predict the coherence time in centimeter-scale cells. In this study we demonstrated, that these models break down in micrometer and sub-micrometer regimes. Cell sizes ranging from mm-scale down to 200 nm did not adhere to prediction based on the standard models. In order to address this shortcoming, we develop an alternative approach better suited for estimating photonic coherence times in ultra-thin vapor cells. This work, highlights the need for a modified theoretical treatment of the coherence time in the nanoscale regime.

Keywords— Nanoscale photonics, Coherence time, Autocorrelation function, Maxwell-Boltzmann

1 Introduction

The second-order intensity autocorrelation function of the optical field, $g^{(2)}(\tau)$ where τ is a time delay, is considered a powerful tool for determining the physical properties of light beams and their sources [1, 2]. It has been used to measure the diameter of a star as Hanbury-Brown and Twiss originally suggested [3–5], to calculate the coherence time and the linewidth of thermal light [6]. In particular, the value of this function at $\tau = 0$ reveals the statistics of the photons: $g^{(2)}(0) = 2$ for Gaussian statistics, $g^{(2)}(0) = 1$ for Poissonian one, and the value $g^{(2)}(0) < 1$ indicates the phenomenon of photon anti-bunching, which is a signature of field non-classicality [2]. Measurements of this function with fully resolved temporal dependence became in the last decade a routine task in quantum information [7–11] and the characterization of a single-photon source such as quantum dot [12], single molecule [13], and diamond color center [14], where its width is in the nanosecond scale.

Recent advances in confining atoms and optical fields at micro- and nanoscale dimensions have opened new avenues for exploring fundamental physics [15–18], developing precision sensors [15, 19, 20], and miniaturizing optical and quantum technologies. One intriguing observation is that the coherence time of light scattered from hot atomic vapor confined in submicron cells increases as the cell thickness decreases. This behavior cannot be explained by conventional models based on the Maxwell-Boltzmann

*Corresponding author: Eliran Talker, elirant@ariel.ac.il

velocity distribution alone. Instead, it requires accounting for additional phenomena such as atomic quenching due to wall collisions, and transit-time broadening.

In this work, we investigate the coherence time of thermal photons in rubidium vapor cells of varying thicknesses, from centimeter-scale down to 200 nm, by measuring the second-order intensity autocorrelation function. Our results reveal a strong dependence of the photon correlation time on cell thickness. While standard models accurately predict the coherence time in centimeter-scale cells, they fail in the micrometer and sub-micrometer regimes. To address this, we develop a refined theoretical framework better suited for estimating photonic coherence times in ultra-thin vapor cells, emphasizing the need for a revised theoretical approach at the nanoscale. The paper is structured as follows: we begin with a theoretical analysis using a Lindblad master equation that incorporates various broadening and shifting mechanisms. We then present our experimental results and discuss their implications. Finally, we conclude with a summary of our findings.

2 Theoretical Background

The second order correlation function of light scattered from an illuminated two-level atom is given by [21]

$$g^{(2)}(\tau) = \frac{G^{(2)}(t, \tau)}{|G^{(1)}(t)|^2} \quad (1)$$

Where $G^{(1)}(\tau) = \langle \hat{E}^-(t) \hat{E}^+(t) \rangle$, and $G^{(2)}(t, \tau) = \langle \hat{E}^-(t) \hat{E}^-(t + \tau) \hat{E}^+(t) \hat{E}^+(t + \tau) \rangle$ the the field operator has an infinite number of degrees of freedom, hence, it might appear complicated to obtain an expression for $E^+(t)$. However, we can take advantage of the existing result which is valid for classically and quantum-mechanically that in the far field regime the emitted field is proportional to the dipole approximation. Omitting negligible constants and, for simplicity, ignoring the vectorial character of the field in the operator we obtain a field that is proportional to the dipole d of the atom at time $t - r/c$.

$$E^{(+)}(r, t) \propto \frac{1}{r} (\rho_{eg}) \left(t - \frac{r}{c} \right)$$

Calculating $G^{(1)}(\tau)$ and $G^{(2)}(t, \tau)$ using the above relation (Equation 1) and quantum regression theorem [22] we can write the correlation function as

$$g^{(2)}(\tau) = \frac{\rho_{22}^{ss}(\tau)}{\rho_{22}^{ss}(\infty)} \quad (2)$$

Where τ is the time delay and ρ_{22}^{ss} is the steady state value of the excited state population. By assuming resonance condition ($\Delta = 0$) and low light intensity limit ($\Omega \rightarrow 0$) we can write the correlation function as (for a full derivation see the Appendix)

$$g^{(2)}(\tau) = 1 + \frac{\Gamma_{eff}^2 \Gamma_2 e^{-\Gamma_{eff}\tau} - \Gamma_{eff}(2\Gamma_2 - \Gamma_{eff})^2 e^{-\Gamma_2\tau}}{(\Gamma_{eff} - \Gamma_2)(2\Gamma_2 + \Gamma_{eff})^2} \quad (3)$$

Where Γ_{eff} is the effective linewidth and is equal to $\Gamma_{eff}^2 \propto \left(\frac{\alpha}{t_{trans}} \right)^2$ with α a unitless factor and t_{trans} is the transit time broadening. Γ_2 is the emission rate which is associated with the relaxation from the excited states to the ground states including radiating and non-radiating process. The first decay element as shown in Equation 3 is $\Gamma_2 = \Gamma_{eff}/2 + \Gamma_{dep}$ where Γ_{dep} is the quenching rate from atom-wall collisions which leads to nonradiative decay from the excited level to the ground state level (see Supplementary). Taking all these decay elements into consideration one can see that the $g^{(2)}(\tau)$ is highly dependent on this parameter and can dramatically reduce the linewidth of the measurements (for more information regarding the theory see Supplementary part II)

3 Experimental Methods

The experimental setup is illustrated in Fig 1.

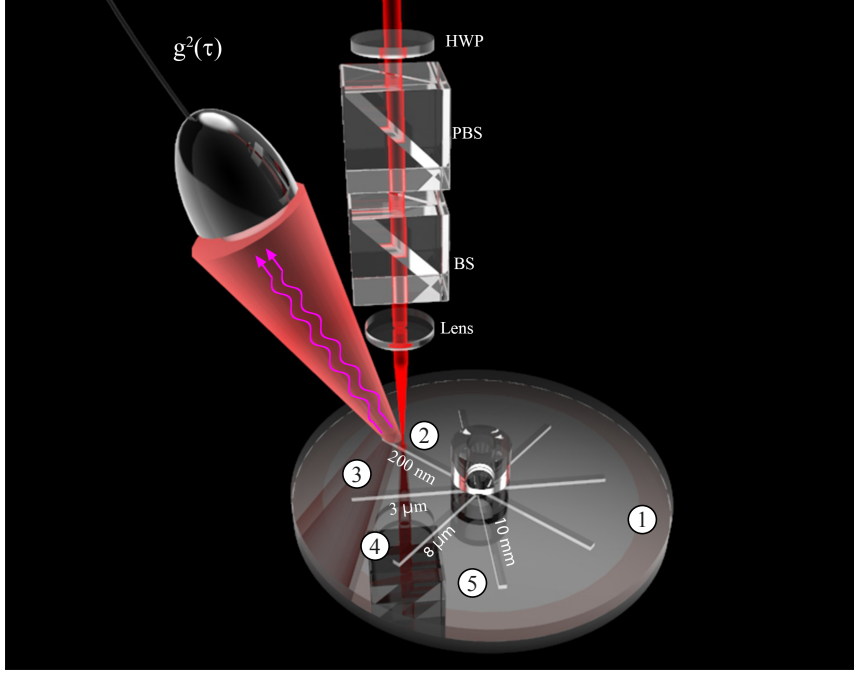


Figure 1: 3D illustration of the experimental setup. The cell is made from 3 channels varying from $8\mu m$ to $200 nm$. The laser beam is stabilized to the close transition $F = 3 \rightarrow F' = 4$, laser beam power $50\mu W$ and the beam waist was set to $\sim 7\mu m$. **HWP** - half wave plate; **PBS** - polarizing beam splitter; **BS** - non-polarizing beam splitter. A schematic layout of our whole setup is presented in the supplementary information.

At the heart of the setup is a vapor cell ① containing three channels with a $10 mm$ length and $1 mm$ width, with the thickness (height) distinguishing between the different channels. In this experiment, the fabricated channel thicknesses were $200 nm$, $3\mu m$, and $8\mu m$ (②, ③, and ④ in Fig. 1 respectively). The cell consists of two borosilicate (pyrex) disks. The first disk in which the channels were fabricated using laser lithography, and etching. Final surface treatment was obtained by reactive ion etching (RIE) followed by deposition of polysilicon on the bonded surfaces. The second disk seals the channels and accommodates the orifice required for evacuating from air and filling of the cells with gas. In the center of the second disk (cover disk), similar in size to the previous one, a hole is drilled and a $4 mm$ ID, glass tube was welded to the cover disk acting as the orifice. The two disks were sealed to each other using anodic bonding. The cell's channels were flushed and evacuated after which they were filled with rubidium vapor and sealed by welding the glass tube. A detailed account regarding the technique can be found here [23]). To this experiment we added 4 Rubidium cells supplied by *Precision Glassblowing Colorado USA* [24] with cell thicknesses of $2 mm$, $5 mm$, $7.5 mm$ and $10 mm$. The cell is placed in a PID temperature controlled oven [25] specifically designed and fabricated by us to avoid introducing any stray magnetic field. Such a magnetic field results naturally from the current flowing through the heating element. The heating element wire consisted of a twisted pair of fine insulated wires with the current through each wire flowing in an opposite direction. Fine micro-welding techniques were employed in fabricating the furnace [26]. A $780 nm$, $100 mW$ laser beam was used as a probe. We used an external cavity diode (laser Toptica DL Pro) passing the beam through a half wave plate followed by a polarizing beam splitter. This allows us to control the beam intensity and improve beam quality and polarization. The polarizer splits the beam by a 90:10 ratio, with the 10% output beam propagating into a saturated absorption spectroscopy (SAS) scheme [27–30] to stabilize the laser frequency to the

closed ($F = 3 \rightarrow F' = 4$) D_2 transition of rubidium 85, mimicking a two level system. Even though we have observed Doppler broadening, our calculations show that a two level system suggests a better agreement with the experimental result. The second 90% of the beam emerging from the beam splitter, passes through a lens obtaining a beam waist of $100\mu\text{m}$ while projecting it on the different channels. The laser output power was set to $50\mu\text{W}$. The scattered light is collected with a single mode fiber (SMF), placed at a distance $L=10$ cm after the cell, at an angle from the beam propagation direction. The scattered light is focused on the SMF using lenses. The distance we set the fiber is chosen such that the conditions for maximum spatial coherence are satisfied [31]. Measuring the second-order intensity autocorrelation is achieved by splitting the fiber coupled light to a 50/50 ratio using a fiber beam splitter, feeding the two beams (branches) to two single-photon avalanche photo diodes (Excelitas, SPCM-800-12-FC). At 780nm the ADP's feature a quantum efficiency of approximately 30%.

4 Experimental results and discussion

The theoretical plot of the second-order autocorrelation intensity as a function of the cell thickness is seen in Figure 2. We observed that by decreasing the cell thickness the linewidth of the $g^{(2)}(\tau)$ measurements are increasing.

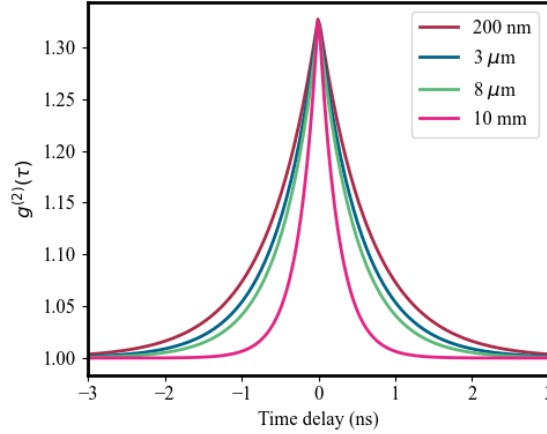


Figure 2: Theoretical plot of the second-order intensity autocorrelation as a function of the cell length, the whole measurements done under low light intensity limit where the Rabi frequency was near zero ($\Omega \rightarrow 0$) and the frequency detuning is set to zero.

The two main factors contributing to the change in the line width, are the mean atomic velocity and the mean free path which are influence by the cell thickness and attributed to the dephasing rate given by [23]

$$\Gamma_{dephase} = \frac{\bar{v}}{\bar{l}} + \frac{v_z}{L/2} \quad (4)$$

Where $\bar{v} = \sqrt{\frac{2k_B T}{m_{Rb}}}$ is the mean atomic velocity, \bar{l} is the mean free path, v_z is the atomic velocity in the direction perpendicular to the cell walls, and L is the cell thickness. The mean free path $\bar{l} = \bar{v}_{rel}/\Gamma_{se}$, where \bar{v}_{rel} is the relative mean thermal velocity if the rubidium atoms, and the rate of spin exchange $\Gamma_{se} = \sigma_{se} \cdot \bar{v}_{rel} \cdot n_{Rb}$, $\sigma_{se} = 2 \times 10^{-14} \text{cm}^2$ is the spin exchange cross section, $\bar{v}_{rel} = \left(\frac{8k_B T}{\pi m_{Rb}}\right)$ is the average relative velocity of the rubidium atoms m_{Rb} is the reduced mass of the system of two rubidium atoms, and n_{Rb} is the density of atoms in the cell (for more information see Supplementary information).

To calculate the unitless factor α which the effective linewidth Γ_{eff} in Equation 3 relates to, we performed a Monte Carlo simulation of thermal atoms traveling within the detection volume. The

simulated results are plotted with the fluorescence spectra obtain from different cell thickness (see supplementary information Part I).

Comparing the theoretical results obtained from Equation 3 to the experimental data (Figure 3), we find excellent agreement with the measurements obtained from different cell thicknesses. The theoretical plotted result was obtained by inserting all the required decay factors into Equation 3. While for mm size cell thicknesses some of the decay factors may be ignored, for cell thicknesses below $50\mu m$ they are required.

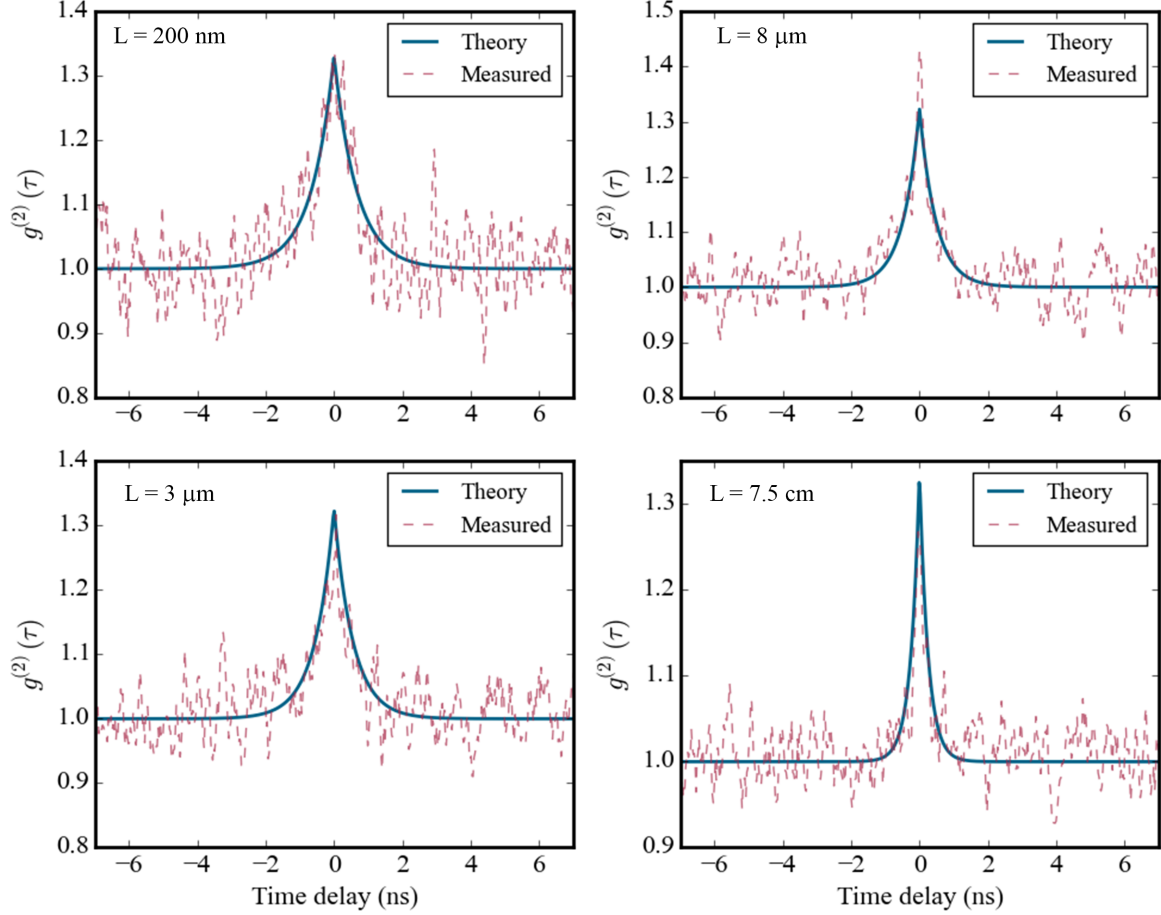


Figure 3: Measurements of the second-order intensity autocorrelation for different cell thickness (a) $200nm$ (b) $3\mu m$ (c) $8\mu m$ (d) 10 mm . The calculated result for the different cell thicknesses, based on Equation 3 is shown to be in excellent agreement.

The transit time broadening calculation was based on a set temperature of $150^{\circ}C$ resulting in an atomic density of approximately $3.5 \times 10^{19}cm^{-3}$, and on a mean speed of 280 m/s .

We find that our simple simulation is sufficient to capture the experimentally observed trend with the unitless factor $\alpha = 8.25$.

We will now turn to calculating the coherence length of the thermal photons

$$L_{co} = c \cdot \tau_{co} \quad (5)$$

Where c is the speed of light and τ_{co} is the coherence time from $g^{(2)}(\tau)$ measurements obtained from both Figure 2 and Figure 3. As demonstrated, we can calculate the coherence length of the thermal light which is scattered from hot rubidium vapor. Simulation based on Equation 3 shows that varying the cell thickness from $100\mu m$ up to $20mm$ the coherence time does not change dramatically with the observed average coherence time being around 0.442 ns (see Supplementary information Equation 32). This changes abruptly, when the cell thickness goes below $8\mu m$ and reaching $3\mu m$ we start to observe

that the average coherence time is doubled (See Figure 4(a)) which implies that we start seeing a limit to the thermal state coherence time as obtained from the Maxwell-Boltzmann derivation.

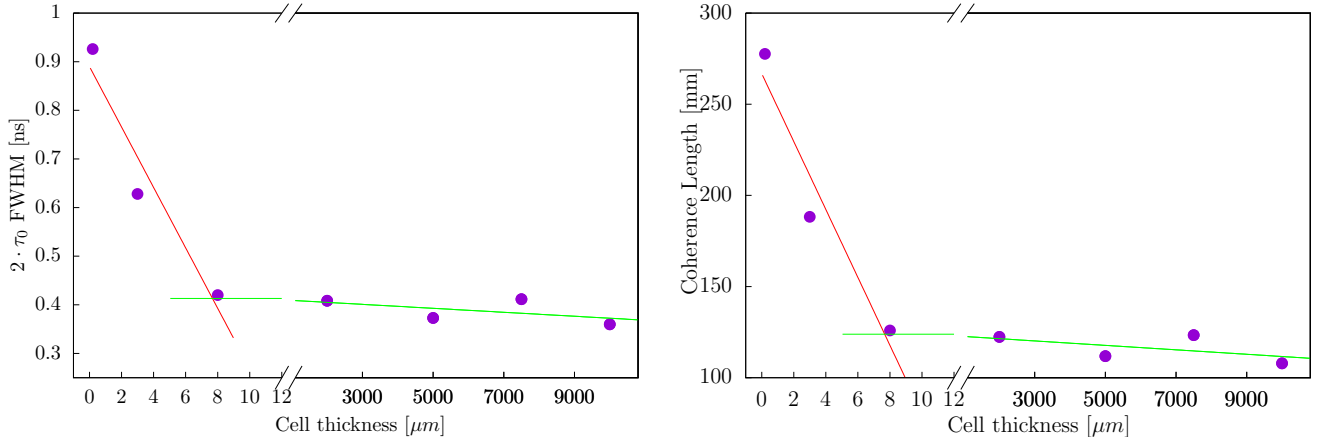


Figure 4: Measured coherence (a) time, as a function of cell length (b) length, as a function of the cell length.

This result corresponds to the fact that if we compare Γ_{eff} to $\Gamma_{dephase}$, $\Gamma_{eff} \approx 2\pi \frac{\alpha}{t_{trans}}$ and $\Gamma_{dephase} \approx \frac{2v_z}{L}$, while taking into account that $t_{trans} = \frac{D}{v}$ (or $\Gamma_{eff} \approx \frac{\alpha \bar{v}}{D}$) we can see that the coherence time of the system depends on the cell thickness compared to the beam waist diameter. As long as $D < L$, Γ_{eff} is dominant and the coherent time is relatively constant. But as L decreases below the beam waist diameter D the coherence time increases. For similar diameters they produced similar coherence times. The best result that we obtained with our rubidium cell is coherence length of around 280 nm. This can be improved if we continue to reduce the cell length and increase the cell temperature leading to an increase in the wall collision rate. This results in an increase of the coherence time. Coherence length and time increase come at a price. The signal to noise ratio decreases since there is a decrease in light-matter interaction, and hence intensity, for the dominant process will be a non-radiative decay due to the quenching effect of the cell walls.

5 Conclusions

We investigated the coherence time of thermal photons in rubidium vapor cells. This work focused on cells with thicknesses ranging from centimeter scale down to 200 nm, revealing a significant dependence on cell thickness. Our measurements of the second-order intensity autocorrelation function, $(g^{(2)}(\tau))$, demonstrated that coherence time increases as cell thickness decreases, particularly in the micrometer and submicrometer regimes. While standard theoretical models based on Maxwell-Boltzmann velocity distributions accurately predict coherence times in larger cells, they fail to account for the observed behavior in cell thicknesses below 8 μm . This discrepancy necessitated a refined theoretical framework incorporating transit-time broadening and atomic quenching due to wall collisions, as described by our Lindblad master equation approach. Our experimental results showed excellent agreement with the proposed model, capturing the impact of cell thickness on linewidth and coherence properties. Notably, for cells below 8 μm , coherence time increased by a factor of two, with the smallest 200 nm cell achieving a coherence length of approximately 290 nm. These findings highlight the limit of the Maxwell-Boltzmann based model of thermal state coherence in confined systems. Also, it underscores the SNR limit of non-radiative decay processes, such as quenching, in nanoscale environments. This work opens new avenues for understanding photon statistics in confined atomic systems, with implications for developing miniaturized quantum technologies, precision sensors, and optical devices. Future

research could explore optimizing cell design, by further reducing thickness or increasing cell temperature, to enhance coherence times. This may come at a price of reduced signal-to-noise ratios due to increased non-radiative decay. These insights provide a foundation for advancing nanoscale photonics and quantum optics applications.

Supplemental Materials: Beyond Maxwell-Boltzmann statistics using confined vapor cells

Part I

Different relaxation effects as a function of cell thickness

The interaction of the atoms with the light is described by the Hamiltonian

$$\frac{d\rho}{dt} = -\frac{i}{\hbar} [\mathcal{H}, \rho] + \mathcal{L}[\rho] \quad (\text{S1})$$

Incorporating the Lindblad operator for the single emitter system into the Hamiltonian [32]

$$\mathcal{L}[\rho] = \sum_{ij} \left(C_{ij} \rho C_{ij}^\dagger - \frac{1}{2} \left(\rho C_{ij}^\dagger C_{ij} + C_{ij}^\dagger C_{ij} \rho \right) \right) \quad (\text{S2})$$

This accounts for both the decay and decoherence of the emitter. The operator has three nonzero terms $C_{ij} \equiv (\Gamma_{spont} + \Gamma_{dephase})|i\rangle\langle j|$, where $|i\rangle$ and $|j\rangle$ represent energy states i and j associated to E_i and E_j respectively, $\Gamma_{spont} + \Gamma_{dephase}$ are the spontaneous emission rates associated with the transition from the excited states to the ground states. $\Gamma_{dephase}$ is a non radiative decay due to wall collisions. We can express the $\Gamma_{dephase}$ as

$$\Gamma_{dephase} = \frac{\bar{v}}{\bar{l}} + \frac{v_z}{L/2} \quad (\text{S3})$$

Where $\bar{v} = \sqrt{\frac{2k_B T}{m_{Rb}}}$ is the most probable velocity, \bar{l} is the mean free path, v_z is the atomic velocity in the direction perpendicular to the cell walls, and L is the cell thickness. The mean free path $\bar{l} = \frac{\bar{v}_{rel}}{\Gamma_{se}}$, where \bar{v}_{rel} is the relative thermal velocity of the rubidium atoms, and the rate of spin exchange $\Gamma_{se} = \sqrt{2} \cdot \sigma_{se} \cdot n_{Rb}$ where $\sigma_{se} = 2 \times 10^{-14} \text{cm}^2$ [] is the spin exchange cross section, $\bar{v} = \left(\frac{4k_B T}{\pi \mu_{Rb}} \right)^{1/2}$ is the average relative velocity of the rubidium atoms (μ_{Rb} is the rubidium atom's mass working temperature of 150°C), and n_{Rb} is the density of atoms in the cell.

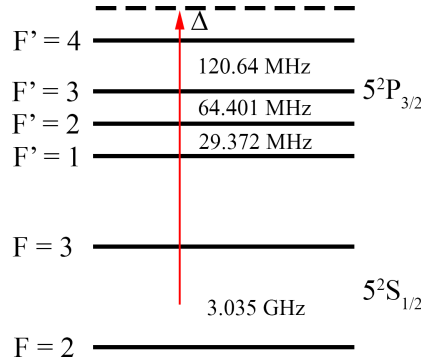


Figure S1: A schematic showing the hyperfine structure and intervals of ^{85}Rb for the D_2 spectroscopic lines

To investigate the effect of relaxation processes as a function of cell thickness, we measured the fluorescence spectra of the D_2 transition (Figure S1) from natural rubidium vapor at a temperature of 150°C . As shown in Figure ??, reducing the cell thickness results in a noticeable decrease in the spectral linewidth. This narrowing can be attributed to the increased frequency of wall collisions, which preferentially filter out faster atoms. Consequently, the signal is dominated by slower atoms, leading

to reduced Doppler broadening. A theoretical model solving Equations S1-S3 while taking the sum of the excited population states and integrating them over the Doppler broadening

$$Fluorescence = \int_{-\infty}^{\infty} \rho_{FF}(\Delta, v) W(v) dv \quad (S4)$$

where $W(v)$ is the one dimensional Maxwellian velocity distribution, which is equal to

$$W(v) = \frac{1}{\sqrt{\pi}u_p} \exp\left(\frac{-v^2}{u_p^2}\right) \quad (S5)$$

$u_p = \sqrt{2k_B T/m}$ is the most probable velocity, k_B is the Boltzmann's constant, m is the mass of rubidium atoms and T is the temperature.

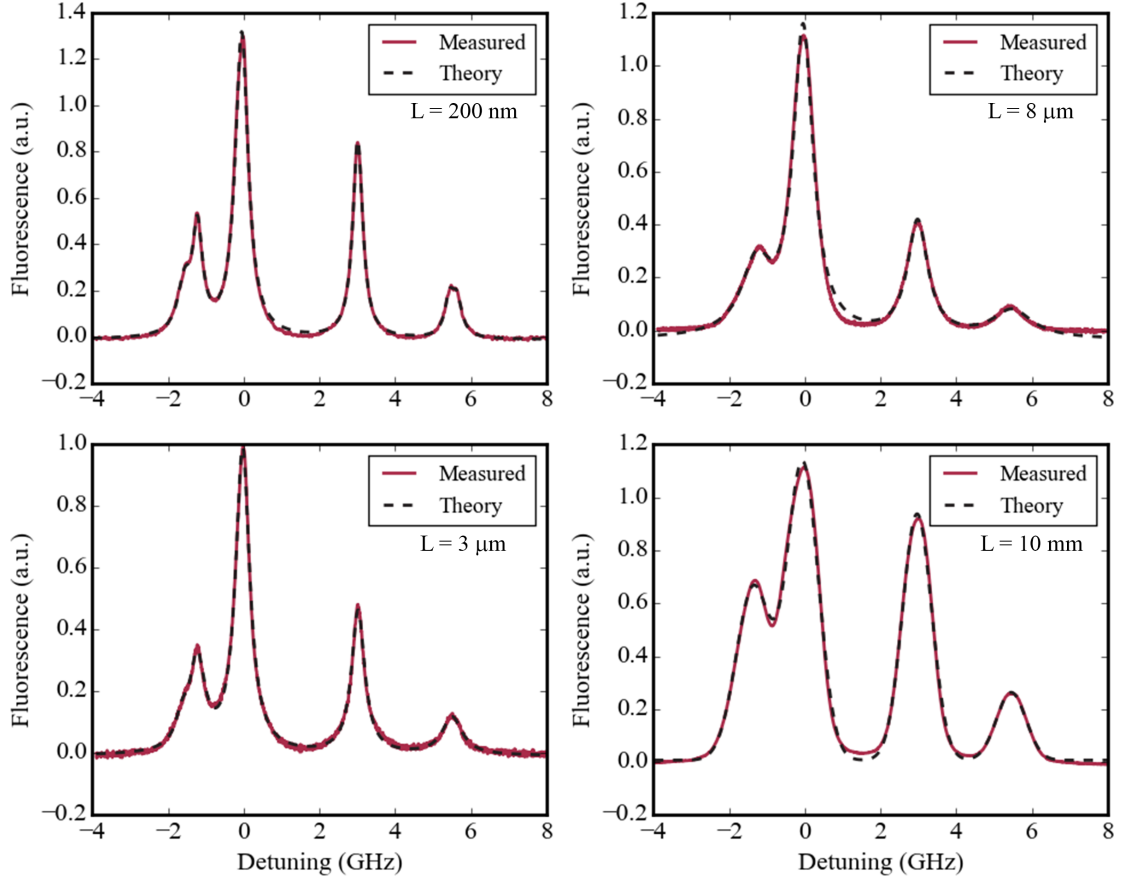


Figure S2: Comparison of fluorescence signal for the D_2 transition as a function of frequency detuning the thin cell of four different values of thickness ($T = 150^\circ\text{C}$).

Part II

$g^2(\tau)$ derivation for submicron cells

The evolution of a damped two-level system, driven at resonances by a coherent field $E_0 \cos(\omega t)$, can be described by the optical Bloch equations [33]

$$\dot{\rho}_{22}(t) = i\frac{\Omega}{2} [\rho_{12}(t) - \rho_{21}(t)] - \Gamma_{eff} \cdot \rho_{22}(t) \quad (S6)$$

$$\dot{\rho}_{21}(t) = i\frac{\Omega}{2} [\rho_{11}(t) - \rho_{22}(t)] - (\Gamma_{eff} - i\Delta)\rho_{21}(t) \quad (S7)$$

$$\dot{\rho}_{12}(t) = (\dot{\rho}_{21}(t))^\dagger \quad (S8)$$

$$1 = \dot{\rho}_{11}(t) + \dot{\rho}_{22}(t)$$

Where Γ_{eff} is define as

$$\Gamma_{eff}^2 = \Gamma_{spont}^2 + \left(\frac{\alpha}{t_{trans}} \right)^2 \quad (S9)$$

Where Γ_{nat} is the natural linewidth ($2\pi \cdot 6$ MHz) and α is unitless factor that attenuates the transit time broadening. This is much lower than the approximate value of $\alpha/t_{trans} \approx 2\pi \cdot 600$ MHz.

The emission rate is given by

$$\Gamma_2 = \Gamma_{eff}/2 + \Gamma_{dephase} \quad (S10)$$

and we defined the Rabi frequency to be $\Omega = d \cdot E/\hbar$. $\rho_{ij}(t)$ are the density matrix elements, with ρ_{11} being the population of the stable lower level, while the upper level population ρ_{22} has a decay rate of $\Gamma_{dephase}$. The off-diagonal density matrix elements are damped at rate Γ_2 , and Δ is the detuning of the optical frequency from the resonant frequency. The time dependence of the interaction has been eliminated by making the rotating wave approximation and transforming to an appropriate interaction picture. The steady state solution of these equations gives the excited-state population as

$$\rho_{22}(\infty) = \frac{1}{2} \frac{\left(\frac{\Omega^2}{\Gamma_{eff} \cdot \Gamma_2} \right)}{1 + \frac{\Delta^2}{\Gamma_2^2} + \left(\frac{\Omega^2}{\Gamma_{eff} \cdot \Gamma_2} \right)} \quad (S11)$$

Since Ω^2 is proportional to the intensity I of the light that drives the excitation, we can express the relation between intensity and Rabi frequency as

$$\frac{\Omega^2}{\Gamma_{eff} \cdot \Gamma_2} = \frac{I}{I_{sat}} \quad (S12)$$

We do not turn to the time dependence of the density matrix which we evaluate here for the special case of resonant excitation ($\Delta = 0$). By solving the coupled differential Equations 6-8

$$\rho_{22}(t) = a_1 + a_2 e^{-\frac{1}{2}(p-q)t} + a_3 e^{-\frac{1}{2}(p+q)t} \quad (S13)$$

Where $p = \Gamma_{eff} + \Gamma_2$, $q = \sqrt{(\Gamma_{depth} - \Gamma_2)^2 - 4\Omega^2}$ and the constants a_1, a_2, a_3 are

$$\{a_1, a_2, a_3\} = \left\{ \frac{2\Omega^2}{p^2 - q^2}, -\frac{\Omega^2}{q(p-q)}, \frac{\Omega^2}{q(P+q)} \right\} \quad (S14)$$

The second order correlation function of the radiation field is defined as [21]

$$g^{(2)} = \frac{\langle I(t) \cdot I(t+\tau) \rangle}{\langle I(t) \rangle^2} \quad (S15)$$

Where $I(t)$ is the intensity operator, and the whole function is expressed in normal ordering. This is the normalized joint probability of detecting a photon at time $t + \tau$, given that another photon was detected at time t . As shown in the main text the second order correlation (Equation 1 in the main article) is equal to

$$g^{(2)}(\tau) = \frac{\rho_{22}(\tau)}{\rho_{22}(\infty)} \quad (S16)$$

Hence the second order correlation at resonance

$$g^{(2)}(\tau) = 1 - \frac{p+q}{2q} e^{-\frac{1}{2}(p-q)\tau} + \frac{p-q}{2q} e^{-\frac{1}{2}(p+q)\tau} \quad (S17)$$

After simplifying the term and by taking the low light intensity limit ($\Omega \rightarrow 0$) we can rewrite the second order correlation as

$$g^{(2)}(\tau) = 1 + \frac{\Gamma_{eff}^2 \Gamma_2 e^{-\Gamma_{eff}\tau} - \Gamma_{eff}(2\Gamma_2 - \Gamma_{eff})^2 e^{-\Gamma_2\tau}}{(\Gamma_{eff} - \Gamma_2)(2\Gamma_2 + \Gamma_{eff})^2} \quad (S18)$$

Part III

Calculation of the coherence time (Numerical approach)

Let's compute the value at $\tau = 0$

$$g^{(2)}(0) = 1 + \frac{\Gamma_{eff}^2 \Gamma_2 - \Gamma_{eff}(2\Gamma_2 - \Gamma_{eff})^2}{(\Gamma_{eff} - \Gamma_2)(2\Gamma_2 + \Gamma_{eff})^2} \quad (S19)$$

Expanding the numerator

$$\begin{aligned} (2\Gamma_2 - \Gamma_{eff})^2 &= 4\Gamma_2^2 - 4\Gamma_{eff}\Gamma_2 + \Gamma_{eff}^2 \\ \Rightarrow \Gamma_{eff}^2 \Gamma_2 - \Gamma_{eff}(2\Gamma_2 - \Gamma_{eff})^2 &= -4\Gamma_{eff}\Gamma_2^2 + 5\Gamma_{eff}^2 \Gamma_2 - \Gamma_{eff}^3 \end{aligned} \quad (S20)$$

Hence, replacing the result in Equation S20 with the numerator of Equation S19

$$g^{(2)}(0) = 1 + \frac{-4\Gamma_{eff}\Gamma_2^2 + 5\Gamma_{eff}^2 \Gamma_2 - \Gamma_{eff}^3}{(\Gamma_{eff} - \Gamma_2)(2\Gamma_2 + \Gamma_{eff})^2} \quad (S21)$$

The peak height above the baseline is

$$\Delta g^{(2)} = g^{(2)}(0) - 1 = \frac{5\Gamma_{eff}^2 \Gamma_2 - 4\Gamma_{eff}\Gamma_2^2 - \Gamma_{eff}^3}{(\Gamma_{eff} - \Gamma_2)(2\Gamma_2 + \Gamma_{eff})^2} \quad (S22)$$

Half the peak height above the baseline is

$$\frac{\Delta g^{(2)}}{2} = \frac{1}{2} \frac{5\Gamma_{eff}^2 \Gamma_2 - 4\Gamma_{eff}\Gamma_2^2 - \Gamma_{eff}^3}{(\Gamma_{eff} - \Gamma_2)(2\Gamma_2 + \Gamma_{eff})^2} \quad (S23)$$

The value of $\frac{1}{2}g^{(2)}(0)$ at half maximum is

$$\frac{1}{2}g^{(2)}(0) = 1 + \frac{\Delta g^{(2)}}{2} = 1 + \frac{1}{2} \frac{5\Gamma_{eff}^2 \Gamma_2 - 4\Gamma_{eff}\Gamma_2^2 - \Gamma_{eff}^3}{(\Gamma_{eff} - \Gamma_2)(2\Gamma_2 + \Gamma_{eff})^2} \quad (S24)$$

In order to find the width at FWHM we find the $\tau > 0$ for which $g^{(2)}(\tau)$ is equal to the expression of the height at half the maximum i.e. $\frac{1}{2}g^{(2)}(0)$ (Equation S24)

$$g^{(2)}(\tau) = 1 + \frac{1}{2} \frac{5\Gamma_{eff}^2 \Gamma_2 - 4\Gamma_{eff}\Gamma_2^2 - \Gamma_{eff}^3}{(\Gamma_{eff} - \Gamma_2)(2\Gamma_2 + \Gamma_{eff})^2} \quad (S25)$$

Substituting $g^{(2)}(\tau)$ with it's expression (Equation S18) and removing the baseline

$$\frac{\Gamma_{eff}^2 \Gamma_2 e^{-\Gamma_{eff}\tau} - \Gamma_{eff}(2\Gamma_2 - \Gamma_{eff})^2 e^{-\Gamma_2\tau}}{(\Gamma_{eff} - \Gamma_2)(2\Gamma_2 + \Gamma_{eff})^2} = \frac{1}{2} \frac{5\Gamma_{eff}^2 \Gamma_2 - 4\Gamma_{eff}\Gamma_2^2 - \Gamma_{eff}^3}{(\Gamma_{eff} - \Gamma_2)(2\Gamma_2 + \Gamma_{eff})^2} \quad (S26)$$

5.1 First case: $L \ll \bar{l}$, $\Gamma_2 \gg \Gamma_{eff}$

The analytical solution of Equation S26 is relatively complex, but by comparing the cell thickness to the mean free path we can simplify the solution. In order to simplify the calculation let's consider a case in which the quenching rate from atom wall collisions $\Gamma_{dephase}$ (Equation S3) is the dominant factor of the emission rate Γ_2 (Equation S10) hence for $\Gamma_2 \gg \Gamma_{eff}$, requires that $\frac{\bar{v}}{l} \ll \frac{v_z}{L/2}$ meaning that the mean free path is much larger than the cell thickness. This assumption becomes valid as our cell thickness decreases into the micron and sub micron. Based on the above assumption we can extract the value of τ at half the peak height, from Equation S26. Reducing the denominator taking into account that $\Gamma_2 \gg \Gamma_{eff}$

$$(\cancel{\Gamma_{eff}} - \Gamma_2)(2\Gamma_2 + \cancel{\Gamma_{eff}})^2 \approx -4\Gamma_2^3$$

Let's examine the left term of Equation S26

$$\frac{\Gamma_{eff}^2 \Gamma_2 e^{-\Gamma_{eff}\tau} - \Gamma_{eff}(2\Gamma_2 - \Gamma_{eff})^2 e^{-\Gamma_2\tau}}{(\Gamma_{eff} - \Gamma_2)(2\Gamma_2 + \Gamma_{eff})^2} \approx \frac{\Gamma_{eff}^2 \Gamma_2 e^{-\Gamma_{eff}\tau} - \Gamma_{eff}(2\Gamma_2 - \cancel{\Gamma_{eff}})^2 e^{-\Gamma_2\tau}}{-4\Gamma_2^3} \approx \quad (S27)$$

$$\approx \cancel{-\frac{1}{4} \frac{\Gamma_{eff}^2}{\Gamma_2^2} e^{-\Gamma_{eff}\tau}} + \frac{\Gamma_{eff}}{\Gamma_2} e^{-\Gamma_2\tau} \quad (S28)$$

where the last term $\frac{\Gamma_{eff}}{\Gamma_2} e^{-\Gamma_2\tau}$ is positive, significantly more dominant, and drops faster than $\frac{\Gamma_{eff}^2}{\Gamma_2^2} e^{-\Gamma_{eff}\tau}$. Hence, replacing this result with the correlation factor in Equation S18 we obtain the reduced second order correlation in ultrathin cells

$$g^{(2)}(\tau) \approx 1 + \frac{\Gamma_{eff}}{\Gamma_2} e^{-\Gamma_2\tau} \quad (S29)$$

Returning to the right term of Equation S26

$$\begin{aligned} \frac{1}{2} \frac{5\Gamma_{eff}^2 \Gamma_2 - 4\Gamma_{eff}\Gamma_2^2 - \Gamma_{eff}^3}{(\Gamma_{eff} - \Gamma_2)(2\Gamma_2 + \Gamma_{eff})^2} &\approx \frac{1}{8} \frac{4\Gamma_{eff}\Gamma_2^2 + \Gamma_{eff}^3 - 5\Gamma_{eff}^2 \Gamma_2}{\Gamma_2^3} = \\ &= \frac{1}{8} \left(\frac{4\Gamma_{eff}}{\Gamma_2} + \frac{\Gamma_{eff}^3}{\Gamma_2^3} - \frac{5\Gamma_{eff}^2}{\Gamma_2^2} \right) \approx \\ &\approx \frac{1}{2} \frac{\Gamma_{eff}}{\Gamma_2} \end{aligned} \quad (S30)$$

we can reduce the higher terms as $1 \gg \Gamma_{eff}/\Gamma_2 \Rightarrow \Gamma_{eff}/\Gamma_2 \gg \Gamma_{eff}^2/\Gamma_2^2 \gg \Gamma_{eff}^3/\Gamma_2^3$. The time delay $\tau_{1/2}$ at half the height of $g^{(2)}(0)$ allows us to evaluate the spread that we can calculate it using the results of Equations S27 and S30

$$\frac{\Gamma_{eff}}{\Gamma_2} e^{-\Gamma_2\tau} = \frac{1}{2} \frac{\Gamma_{eff}}{\Gamma_2}$$

$$e^{-\Gamma_2\tau} = 2^{-1}$$

$$\Gamma_2\tau = \ln 2$$

$$\Rightarrow \tau = \frac{\ln 2}{\Gamma_2}$$

As the linewidth is twice $\tau_{1/2}$

$$FWHM = \frac{2 \ln 2}{\Gamma_2} \propto \frac{1.386}{v_z} \cdot L \quad (S31)$$

5.2 Second case: $\Gamma_{eff} \gg \Gamma_{dephase}$

When dealing with large cell thicknesses, non radiative decay due to wall collisions is negligible compared to the effective decay hence the emission rate (Equation S10) is approximately

$$\Gamma_2 \approx \frac{\Gamma_{eff}}{2}$$

the denominator of Equation S26 becomes

$$(\Gamma_{eff} - \Gamma_2)(2\Gamma_2 + \Gamma_{eff})^2 \approx \frac{1}{2}\Gamma_{eff}(2\Gamma_{eff})^2 = 2\Gamma_{eff}^3$$

the right side of Equation S26 becomes

$$\frac{1}{2} \frac{\frac{5}{2}\Gamma_{eff}^3 - 2\Gamma_{eff}^3 - \Gamma_{eff}^3}{2\Gamma_{eff}^3} = \frac{5}{8}$$

and the left side of Equation S26

$$\begin{aligned} & \approx \frac{1}{2} \frac{\cancel{\Gamma_{eff}^2} \cdot \frac{1}{2}\cancel{\Gamma_{eff}} \cdot e^{\Gamma_{eff}\tau} - \Gamma_{eff}(\Gamma_{eff} - \cancel{\Gamma_{eff}})^2 e^{-\frac{1}{2}\Gamma_{eff}\tau}}{2\cancel{\Gamma_{eff}^3}} = \frac{1}{4}e^{-\Gamma_{eff}\tau} \\ & \frac{1}{4}e^{-\Gamma_{eff}\tau} = \frac{5}{8} \\ & \Gamma_{eff}\tau = \ln 5 - \ln 2 = 0.9163 \end{aligned}$$

given that $\Gamma_{eff} \approx 2\pi \times \frac{\alpha \bar{v}}{D} = 2\pi \times 200 \times 10^6 \text{ Hz}$ for values of $\alpha = 8.25$, $\bar{v} = 280 \text{ m/s}$, $D = 7 \mu\text{m}$.

$$\tau \approx \frac{0.9163}{\Gamma_{eff}} = 4.419 \times 10^{-10} \text{ s} \quad (\text{S32})$$

Part IV

Detailed description of the experimental setup

The full experimental setup, illustrated in Fig. S4, was used throughout the experiment. A Toptica DL pro laser operating at 780 nm with an output power of 80 mW provided the required spatial and temporal stability for the beam entering the thin vapor cell. To suppress beam jitter and eliminate higher-order spatial modes, the laser beam was passed through a high-finesse, three-mirror ring cavity acting as a mode cleaner. The incident beam typically includes significant contributions from higher-order modes—particularly first- and second order which distort the beam profile. The length of the cavity was adjusted to ensure resonance only for the fundamental TEM₀₀ mode.

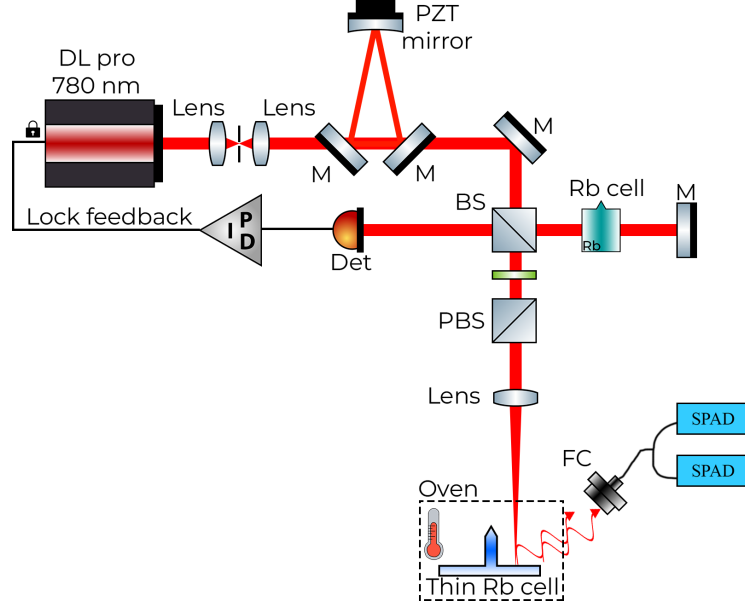


Figure S3: Experimental setup used for the intensity auto-correlation measurements for our thin cell. M: mirror; PBS: polarizing beam splitter; FC: fiber collimator; Det: detector.

In addition to the mode-cleaner cavity, a spatial filter composed of two lenses and an iris was used to further improve the beam quality. The laser beam was then split into two paths: one arm was directed to a saturated absorption spectroscopy setup for frequency stabilization, while the second arm was directed toward the experiment. This beam passed through a half-wave plate and a polarizing beam splitter to control its intensity and ensure clean linear polarization. After focusing the beam into the vapor cell using a lens, the fluorescence signal was collected with a fiber collimator. The collected light was then split via a fiber splitter and directed to two single-photon detectors, enabling measurement of the fluorescence intensity auto-correlation function.

References

- [1] Roy J Glauber. The quantum theory of optical coherence. *Physical Review*, 130(6):2529, 1963.
- [2] Leonard Mandel and Emil Wolf. *Optical coherence and quantum optics*. Cambridge university press, 1995.
- [3] Rodney Loudon. *The quantum theory of light*. OUP Oxford, 2000.
- [4] R Hanbury Brown and Richard Q Twiss. Correlation between photons in two coherent beams of light. *Nature*, 177(4497):27–29, 1956.
- [5] R Hanbury Brown and Richard Q Twiss. Lxxiv. a new type of interferometer for use in radio astronomy. *The London, Edinburgh, and Dublin Philosophical Magazine and Journal of Science*, 45(366):663–682, 1954.
- [6] FT Arecchi, A Berne, and A Sona. Measurement of the time evolution of a radiation field by joint photocount distributions. *Physical Review Letters*, 17(5):260, 1966.
- [7] Jonas S Neergaard-Nielsen, B Melholt Nielsen, C Hettich, Klaus Mølmer, and Eugene S Polzik. Generation of a superposition of odd photon number states for quantum information networks. *Physical review letters*, 97(8):083604, 2006.

- [8] Jonas S Neergaard-Nielsen, Yujiro Eto, Chang-Woo Lee, Hyunseok Jeong, and Masahide Sasaki. Quantum tele-amplification with a continuous-variable superposition state. *Nature Photonics*, 7(6):439–443, 2013.
- [9] Ranjit Singh and Alexander E Teretenkov. Quantum sensitivity of squeezed schrodinger cat states. *Physics Open*, 18:100198, 2024.
- [10] Kan Takase, Fumiya Hanamura, Hironari Nagayoshi, J Eli Bourassa, Rafael N Alexander, Akito Kawasaki, Warit Asavanant, Mamoru Endo, and Akira Furusawa. Generation of flying logical qubits using generalized photon subtraction with adaptive gaussian operations. *Physical Review A*, 110(1):012436, 2024.
- [11] Demid V Sychev, Alexander E Ulanov, Anastasia A Pushkina, Matthew W Richards, Ilya A Fedorov, and Alexander I Lvovsky. Enlargement of optical schrödinger’s cat states. *Nature Photonics*, 11(6):379–382, 2017.
- [12] Yasuhiko Arakawa and Mark J Holmes. Progress in quantum-dot single photon sources for quantum information technologies: a broad spectrum overview. *Applied Physics Reviews*, 7(2), 2020.
- [13] C Toninelli, I Gerhardt, AS Clark, A Reserbat-Plantey, Stephan Götzinger, Z Ristanović, M Colautti, P Lombardi, KD Major, I Deperasińska, et al. Single organic molecules for photonic quantum technologies. *Nature Materials*, 20(12):1615–1628, 2021.
- [14] Marcus W Doherty, Neil B Manson, Paul Delaney, Fedor Jelezko, Jörg Wrachtrup, and Lloyd CL Hollenberg. The nitrogen-vacancy colour centre in diamond. *Physics Reports*, 528(1):1–45, 2013.
- [15] Eliran Talker, Pankaj Arora, Yefim Barash, David Wilkowski, and Uriel Levy. Efficient optical pumping of alkaline atoms for evanescent fields at dielectric-vapor interfaces. *Optics Express*, 27(23):33445–33458, 2019.
- [16] Eliran Talker, Liron Stern, Alex Naiman, Yefim Barash, and Uriel Levy. Fluorescence double resonance optical pumping spectrum and its application for frequency stabilization in millimeter scale vapor cells. *Journal of Physics Communications*, 1(5):055016, 2017.
- [17] James Keaveney, Armen Sargsyan, Ulrich Krohn, Ifan G Hughes, David Sarkisyan, and Charles S Adams. Cooperative lamb shift in an atomic vapor layer of nanometer thickness. *Physical review letters*, 108(17):173601, 2012.
- [18] J Delpy, N Fayard, F Bretenaker, and F Goldfarb. Anomalous high-density spin noise in a strongly interacting atomic vapor. *Physical Review Research*, 7(1):013298, 2025.
- [19] Clément Carlé, Michael Petersen, Nicolas Passilly, Moustafa Abdel Hafiz, Emeric de Clercq, and Rodolphe Boudot. Exploring the use of ramsey-cpt spectroscopy for a microcell-based atomic clock. *IEEE Transactions on Ultrasonics, Ferroelectrics, and Frequency Control*, 68(10):3249–3256, 2021.
- [20] Xiaochi Liu, Jean-Marc Merolla, Stéphane Guérandel, Emeric De Clercq, and Rodolphe Boudot. Ramsey spectroscopy of high-contrast cpt resonances with push-pull optical pumping in cs vapor. *Optics express*, 21(10):12451–12459, 2013.
- [21] Miguel Orszag. *Quantum optics: including noise reduction, trapped ions, quantum trajectories, and decoherence*. Springer Nature, 2024.
- [22] Sakil Khan, Bijay Kumar Agarwalla, and Sachin Jain. Quantum regression theorem for multi-time correlators: a detailed analysis in the heisenberg picture. *Physical Review A*, 106(2):022214, 2022.

- [23] Eliran Talker, Roy Zektzer, Yefim Barash, Noa Mazurski, and Uriel Levy. Atomic spectroscopy and laser frequency stabilization with scalable micrometer and sub-micrometer vapor cells. *Journal of Vacuum Science & Technology B*, 38(5), 2020.
- [24] Precision Glassblowing of Colorado U.S.A. Gas wavelength reference cells. 2025. URL: <https://precisionglassblowing.com/gas-wavelength-reference-cells/>.
- [25] Gilad Orr, Paul Ben Ishai, and Michael Roth. High-temperature time domain measurement system for solid and molten materials. *Measurement Science and Technology*, 29(10):105502, 2018.
- [26] Gilad Orr and Michael Roth. Safe and consistent method of spot-welding platinum thermocouple wires and foils for high temperature measurements. *Review of scientific instruments*, 83(8), 2012.
- [27] JE Debs, NP Robins, A Lance, MB Kruger, and JD Close. Piezo-locking a diode laser with saturated absorption spectroscopy. *Applied optics*, 47(28):5163–5166, 2008.
- [28] Jian-Hong Wan, Chang Liu, and Yan-Hui Wang. Laser frequency locking based on the normal and abnormal saturated absorption spectroscopy of 87rb. *Chinese Physics B*, 25(4):044204, 2016.
- [29] U Dammalapati, I Norris, and E Riis. Saturated absorption spectroscopy of calcium in a hollow-cathode lamp. *Journal of Physics B: Atomic, Molecular and Optical Physics*, 42(16):165001, 2009.
- [30] Shang-qing Liang, Yun-fei Xu, and Qiang Lin. Laser frequency locking with low pump field saturated absorption spectroscopy. *Journal of Zhejiang University-SCIENCE A*, 19(2):171–174, 2018.
- [31] Kazuyuki Nakayama, Yutaka Yoshikawa, Hisatoshi Matsumoto, Yoshio Torii, and Takahiro Kuga. Precise intensity correlation measurement for atomic resonance fluorescence from optical molasses. *Optics express*, 18(7):6604–6612, 2010.
- [32] Heinz-Peter Breuer and Francesco Petruccione. *The theory of open quantum systems*. OUP Oxford, 2002.
- [33] Heung-Ryoul Noh and Wonho Jhe. Analytic solutions of the optical bloch equations. *Optics communications*, 283(11):2353–2355, 2010.